PCCP

PAPER

View Article Online
View Journal | View Issue



Cite this: *Phys. Chem. Chem. Phys.*, 2016, **18**, 12278

# $Na^+$ doping induced changes in the reduction and charge transport characteristics of $Al_2O_3$-stabilized, CuO-based materials for $CO_2$ capture†

Q. Imtiaz,[a] P. M. Abdala,[a] A. M. Kierzkowska,[a] W. van Beek,[b] S. Schweiger,[c] J. L. M. Rupp[c] and C. R. Müller*[a]

Chemical looping combustion (CLC) and chemical looping with oxygen uncoupling (CLOU) are emerging $CO_2$ capture technologies that could reduce appreciably the costs associated with the capture of $CO_2$. In CLC and CLOU, the oxygen required to combust a hydrocarbon is provided by a solid oxygen carrier. Among the transition metal oxides typically considered for CLC and CLOU, copper oxide (CuO) stands out owing to its high oxygen carrying capacity, exothermic reduction reactions and fast reduction kinetics. However, the low Tammann (sintering) temperature of CuO is a serious drawback. In this context, it has been proposed to support CuO on high Tammann temperature and low cost alumina ($Al_2O_3$), thus, reducing the morphological changes occurring over multiple CLC or CLOU redox cycles and stabilizing, in turn, the high activity of CuO. However, in CuO–$Al_2O_3$ systems, phase stabilization and avoiding the formation of the $CuAl_2O_4$ spinel is key to obtaining a material with a high redox stability and activity. Here, we report a $Na^+$ doping strategy to phase stabilize $Al_2O_3$-supported CuO, yielding in turn an inexpensive material with a high redox stability and $CO_2$ capture efficiency. We also demonstrate that doping CuO–$Al_2O_3$ with $Na^+$ improves the oxygen uncoupling characteristics and coke resistance of the oxygen carriers. Utilizing *in situ* and *ex situ* X-ray absorption spectroscopy (XAS), the local structure of Cu and the reduction pathways of CuO were determined as a function of the $Na^+$ content and cycle number. Finally, using 4-point conductivity measurements, we confirm that doping of $Al_2O_3$-supported CuO with $Na^+$ lowers the activation energy for charge transport explaining conclusively the improved redox characteristics of the new oxygen carriers developed.

Received 13th January 2016,
Accepted 23rd March 2016

DOI: 10.1039/c6cp00257a

www.rsc.org/pccp



## Introduction

Chemical looping combustion (CLC) and chemical looping with oxygen uncoupling (CLOU) are emerging $CO_2$ capture and storage (CCS) technologies that could substantially reduce the costs that are associated with the capture of $CO_2$.[1,2] In CLC, lattice oxygen of an oxygen carrier, typically a transition metal oxide, is used to combust a hydrocarbon. For example, the full oxidation of methane ($CH_4$) with oxygen provided by copper oxide (CuO) is given as

$$CH_4 + 4CuO \rightarrow CO_2 + 2H_2O + 4Cu \quad (1)$$

Chemical looping with oxygen uncoupling (CLOU) is an extension of the CLC process to efficiently combust solid fuels. In CLOU a hydrocarbon is combusted with molecular oxygen that is derived from a metal oxide *via* a reduction reaction, *viz.*

$$4CuO \rightarrow 2Cu_2O + O_2(g) \quad (2)$$

$$CH_4 + 2O_2(g) \rightarrow CO_2 + 2H_2O \quad (3)$$

After the condensation of steam, a pure stream of $CO_2$ is obtained, which can be readily compressed and sequestered. The advantage of CLOU over CLC is that a solid fuel, *e.g.* coal can be combusted directly, *i.e.* an intermediate, often rate-limiting gasification step is omitted. To close the cycle, the reduced oxygen carrier is re-oxidized in air:

$$2Cu_2O + O_2 \rightarrow 4CuO \quad (4a)$$

or

$$2Cu + O_2 \rightarrow 2CuO \quad (4b)$$

[a] *Laboratory of Energy Science and Engineering, Department of Mechanical and Process Engineering, ETH Zürich, Leonhardstrasse 21, 8092 Zürich, Switzerland. E-mail: muelchri@ethz.ch*
[b] *Swiss Norwegian Beamlines, European Synchrotron Radiation Facility (ESRF), Grenoble, France*
[c] *Electrochemical Materials, Department of Materials, ETH Zürich, Hönggerbergring 64, 8093 Zürich, Switzerland*

† Electronic supplementary information (ESI) available. See DOI: 10.1039/c6cp00257a

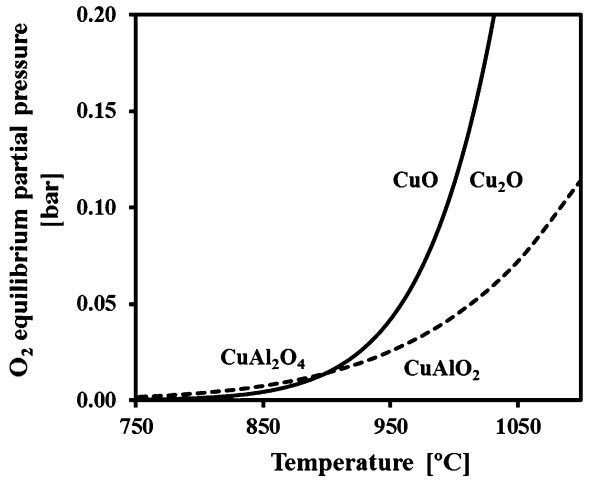


Fig. 1 The equilibrium partial pressure of $O_2$ as a function of temperature: (—) CuO–$Cu_2O$ couple and (– –) $CuAl_2O_4$–$CuAlO_2$ couple. The thermodynamic data was taken from Barin and Knacke,[7] and Jacob and Alcock.[8]

The oxidation reaction (4), is always exothermic, whereas the reduction reaction (1) is commonly endothermic, the most prominent exception being CuO. During CLC and CLOU operation, the two reaction steps, *i.e.* the reduction and re-oxidation of the oxygen carrier, are separated either spatially or temporally. Therefore, in CLC and CLOU the effluent during the combustion reaction is not diluted with nitrogen and, hence, the costs associated with the energy intensive $CO_2$ separation step are avoided. A further advantage of CLC and CLOU over conventional combustion processes is that the formation of $NO_x$ is largely reduced.

The CuO–$Cu_2O$/Cu redox couple has been identified as a very attractive material for CLC and CLOU owing to its (i) high oxygen carrying capacity of 0.2 g $O_2$ per g CuO under CLC conditions, (ii) high oxygen uncoupling capacity of 0.1 g $O_2$ per g CuO under CLOU conditions, (iii) high equilibrium oxygen partial pressure in the temperature range 850–1000 °C (see Fig. 1), (iv) fast kinetics for the reduction reactions and (v) exothermic reduction reaction. However, the Tammann temperatures of CuO, $Cu_2O$ and Cu (526 °C, 481 °C and 405 °C, respectively) are significantly lower than the typical operating temperature of the CLC and CLOU processes (850–1000 °C). The Tammann temperature indicates the onset of sintering and is defined empirically as half of the melting temperature, $T_m$ (in Kelvin). Thus, research efforts are currently directed towards the development of sintering resistant CuO-based oxygen carriers that possess high phase stability and in turn also a high redox activity and stability. Various high Tammann temperature supports, *e.g.* $ZrO_2$, $Al_2O_3$, $TiO_2$, $SiO_2$ or $MgAl_2O_4$ have been proposed.[3] Among the different support materials, $Al_2O_3$ has received most attention owing to its low cost and high Tammann temperature of $\sim$885 °C.[1,4–6]

The phase diagram of the $Cu_2O$–CuO–$Al_2O_3$ system shows that at temperatures exceeding 600 °C $Al_2O_3$ can form a solid solution with CuO, *viz.* the spinel ($CuAl_2O_4$) or delafossite ($CuAlO_2$).[8] Chuang *et al.*[9] and Imtiaz *et al.*[10] demonstrated previously that CuO that is present in the spinel phase is fully reducible under CLC conditions. Therefore, the formation of $CuAl_2O_4$ does not reduce the oxygen carrying capacity of $Al_2O_3$-stabilized CuO. However, the formation of $CuAl_2O_4$ does affect negatively the CLOU performance of $Al_2O_3$-stabilized CuO owing to the irreversible decomposition of $CuAl_2O_4$ to $CuAlO_2$ and the low oxygen equilibrium partial pressure of the $CuAl_2O_4$–$CuAlO_2$ couple (Fig. 1).[11]

A strategy to avoid the reaction between $Al_2O_3$ and transition metal oxides is doping with small quantities of alkali metal ions (*e.g.* $Li^+$, $Na^+$ or $K^+$). For example, Houalla *et al.*[12] showed that $Al_2O_3$ and NiO did not form $NiAl_2O_4$ when doped with $Li^+$. The inhibition of $NiAl_2O_4$ formation was explained by the preferential formation of an $Al_2O_3$–Li spinel. Using X-ray diffraction and differential thermal analysis, El-Shobaky *et al.*[13] studied the solid–solid reaction between CuO (16.3 wt%) and $Na^+$-doped $Al_2O_3$ in the temperature range 500–1000 °C. It was observed that the presence of $Na^+$ prevented the reaction between CuO and $Al_2O_3$. This was attributed to the formation of a sodium aluminate phase at the surface of the $Al_2O_3$ grains. El-Shobaky *et al.*[13] speculated that the sodium-aluminate phase limited the thermal diffusion of $Cu^{2+}$ into the $Al_2O_3$ matrix, thus, preventing the formation of the copper aluminate spinel. In a previous study, Imtiaz *et al.*[14] reported that the incorporation of $K^+$ in the CuO–$Al_2O_3$ matrix did not only avoid the formation of the spinel $CuAl_2O_4$ but also reduced the propensity of the material to coke deposition.

However, the effect of alkali metals on the structural characteristics and cyclic redox performance of $Al_2O_3$-stablized, CuO-based oxygen carriers is currently unknown. In addition, the reduction pathways of commercial, pure (*i.e.* unsupported) CuO have been probed only at low temperatures (200–300 °C).[15] Thus, the aim of the present study is to investigate the influence of $Na^+$ doping on the reduction, oxygen uncoupling and coke deposition characteristics of $Al_2O_3$-stabilized, CuO-based oxygen carriers. To achieve a homogeneous distribution of the dopant ($Na^+$), a sol–gel technique was utilized. The quantity of CuO in the oxygen carriers was fixed to 70 wt%. The structure and reduction pathways of $Na^+$-doped, $Al_2O_3$-stabilized, CuO were studied at 750 °C using X-ray absorption spectroscopy (XAS). In addition, the effect of $Na^+$ doping on charge transport was also probed.

# Experimental

### Oxygen carrier synthesis

$Na^+$-doped (1, 3 or 5 wt%), $Al_2O_3$-stabilized, CuO-based (70 wt% CuO) oxygen carriers were synthesized using a sol–gel technique. In a typical synthesis, first an appropriate amount of aluminium isopropoxide ($(C_3H_7O)_3Al$) was added to deionized water. The obtained mixture was heated to 75 °C and allowed to hydrolyse for 0.5 h under stirring. Subsequently, the solution was peptized with concentrated nitric acid. The molar ratio of $Al^{3+}:H_2O:H^+$ was 0.5 : 50 : 0.07.[16] After peptization, condensation was allowed for 2 h at 90 °C. Subsequently, an aqueous solution containing appropriate amounts of copper(II) nitrate ($Cu(NO_3)_2{\cdot}2.5H_2O$) and sodium hydroxide (NaOH) was added to the aluminium gel.

The mixture was heated under reflux for 12 h at 90 °C and subsequently dried at 100 °C. The final oxygen carrier was obtained by calcination in air in a muffle furnace at 900 °C for 2 h (temperature ramp 5 °C $min^{-1}$). Throughout this paper, the abbreviation CuAlNax, where $x$ is the wt% of $Na^+$, will be used to refer to the different oxygen carriers synthesized.

### Characterization techniques

A Bruker D8 Advance diffractometer, equipped with a Lynx eye super speed detector, was used to analyse the composition and crystallinity of (i) freshly calcined, (ii) reduced and (iii) cycled oxygen carriers. The diffractometer was operated at 40 mA and 40 kV using Cu $K_\alpha$ radiation. Each sample was scanned in the range $2\theta = 20°–80°$. The step size was 0.0275° and the scan time per step was 0.8 s. A scanning electron microscope (FEI Magellan 400 FEG) was used to characterize the surface morphology of the freshly calcined oxygen carriers. A double-sided carbon tape was used to attach samples of the oxygen carrier onto an aluminium holder. Prior to imaging, the samples were sputter coated with an approximately 3 nm thick layer of platinum. The surface area and pore volume of the synthesized oxygen carriers were determined using a Quantachrome NOVA 4000e analyser. Prior to the acquisition of the $N_2$ isotherms at −196 °C, each sample was degassed at 300 °C for approximately 3 h. The Brunauer *et al.*[17] (BET) and the Barrett *et al.*[18] (BJH) models were used to calculate, respectively, the surface area and the pore volume of the freshly calcined materials from the acquired isotherms.

The electrical conductivity and the activation energy for charge transport were determined by 4-point conductivity measurements on sintered pellets.[19,20] The materials were first crushed and then pelletized *via* uniaxial (40 kN for 2 min) and isostatic (1000 kN for 2 min) pressing. The pellets were sintered in air ($P_{O_2}$ = 0.21 bar) for 24 h at 1000 °C (the heating and cooling rate was 3 °C $min^{-1}$). The sintered pellets possessed a density of >95% of the theoretical bulk density. Platinum electrodes were applied in a 4-point electrode arrangement on both sides of the pellets (Heraeus 3605). The resistance of each pellet was measured in air as a function of temperature (from 25 °C to 950 °C using a heating and cooling rate of 3 °C $min^{-1}$) by applying a DC voltage of 1 V (Keithley 2601B multimeter). To ensure reproducibility, three heating and cooling cycles were performed.

To determine the oxygen uncoupling characteristics and the CuO content of the synthesized oxygen carriers, $N_2$-temperature programmed reduction (TPR) experiments were performed in a thermo-gravimetric analyser (TGA, Mettler Toledo TGA/DSC 1). In a typical experiment, ~15 mg of the oxygen carrier were heated from 25 °C to 1150 °C with a rate of 10 °C $min^{-1}$ under a flow of $N_2$ (25 mL $min^{-1}$). $H_2$- and $CH_4$-TPR were performed to probe, respectively, the reduction characteristics and the propensity for coke formation of the synthesized oxygen carriers. In a typical experiment, ~15 mg of the oxygen carrier was heated from 25 °C to 1000 °C at a rate of 10 °C $min^{-1}$. At the end of the temperature ramp the material was kept at 1000 °C for an additional 30 min. $H_2$-TPR and $CH_4$-TPR experiments were performed using 5 vol% $H_2$ in $N_2$ and 10 vol% $CH_4$ in $N_2$, respectively. A Philips CM12 transmission electron microscope, operated at 100 kV, was used to image the carbon deposited.

### Cyclic CLC and CLOU performance

The cyclic oxygen carrying capacity of the synthesized oxygen carriers was studied in a TGA at 900 °C. A mixture of 10 vol% $CH_4$ in $N_2$ was used for reduction (CLC), whereas a $N_2$ atmosphere was used for CLOU experiments. The reduced materials were re-oxidized with air. In each reaction segment, the flow rate of the gases was 25 mL $min^{-1}$ (25 °C and 1 bar). In addition, a constant $N_2$ flow of 25 mL $min^{-1}$ was used as purge flow over the micro-balance. In a typical experiment, a small quantity (~25 mg) of the oxygen carrier was placed in an alumina pan and heated from room temperature to 900 °C (10 °C $min^{-1}$) in a flow of air. After reaching the reaction temperature, a reduction step was performed. The duration of the reduction steps during CLC and CLOU experiments was 390 s and 600 s, respectively. Subsequently, the oxygen carrier was re-oxidized in air. The oxygen carriers were re-oxidized for 390 s and 600 s for CLC and CLOU operation, respectively. In CLC experiments a $N_2$ flow was used to purge the reaction chamber for 60 s between each reduction and oxidation segment. The reduction and oxidation cycle was repeated 20 times.

### X-ray absorption spectroscopy

X-ray absorption spectroscopy (XAS) was performed at the Swiss-Norwegian beamline (BM01B) at the European Synchrotron Radiation Facility (ESRF), Grenoble, France. The measurements (Cu K-edge) were performed in transmission mode using a Si(111) double crystal monochromator. The energy was calibrated to the edge position of Cu foil (8979 eV). In order to study the local atomic order in the materials developed, extended X-ray absorption fine structure (EXAFS) data were collected (pellets using cellulose as binder). *In situ* X-ray absorption near edge structure (XANES) spectroscopy was performed to determine the reduction pathways of two representative oxygen carriers, *viz.* CuAlNa0 and CuAlNa5. A detailed description of the experimental set-up used for the XAS measurements is given in the ESI.† XAS data normalization and analysis were performed using the Athena and Artemis software packages (Demeter 0.9.20 software package).[21] The structural parameters, such as interatomic distances, coordination number and the Debye–Waller factor, were obtained by nonlinear least-squares fitting of the acquired EXAFS data ($k^3$-weighted, $k$-range 3–13 $Å^{-1}$).

## Results

### Characterization of the calcined oxygen carriers

Fig. 2 shows the X-ray diffractograms of the calcined oxygen carriers. CuAlNa0 and CuAlNa1 contained CuO and $CuAl_2O_4$, whereas CuAlNa3 and CuAlNa5 contained only CuO and $NaAlO_2$ (minor phase). The absence of $CuAl_2O_4$ in CuAlNa3 and CuAlNa5 is most likely due to $Na^+$ suppressing the formation of the spinel. Due to the lack of diffraction peaks for $Al_2O_3$ in CuAlNa3 and CuAlNa5, $Al_2O_3$ is most likely present in an amorphous form.

 

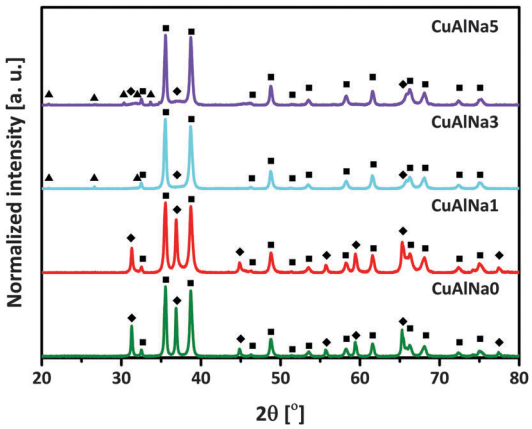


Fig. 2 X-ray diffractograms of the calcined oxygen carriers. The following compounds were identified: (■) CuO, (◆) $CuAl_2O_4$ and (▲) $NaAlO_2$.

Table 1 Average crystallite size and the weight fraction of CuO and $CuAl_2O_4$ ($Al_2O_3$-free basis) in the calcined oxygen carriers. The average crystallite sizes were calculated from the (200) and (311) reflections of CuO and $CuAl_2O_4$, respectively. The weight fractions of the $Cu^{2+}$-containing phases were determined from the XANES spectra using LCF

| Material | CuO [nm] | $CuAl_2O_4$ [nm] | CuO [—] | $CuAl_2O_4$ [—] |
|---|---|---|---|---|
| CuAlNa0 | 23 | 38 | 0.71 ± 0.03 | 0.29 ± 0.03 |
| CuAlNa1 | 21 | 34 | 0.75 ± 0.03 | 0.25 ± 0.03 |
| CuAlNa3 | 24 | — | 0.91 ± 0.03 | 0.09 ± 0.03 |
| CuAlNa5 | 25 | — | 0.98 ± 0.02 | 0.02 ± 0.02 |

From Table 1 it can be seen that the average crystallite size of CuO in the synthesized oxygen carriers, estimated using the Scherrer equation,[22] is ~23 nm (independent of the fraction of $Na^+$).

XANES and EXAFS spectroscopy were performed to gain a better insight into the local Cu environment. Fig. 3(a) plots the Cu K-edge XANES spectra (acquired at room temperature) of the synthesized materials. For comparison, the Cu K-edge XANES spectra of pure, *i.e.* unsupported CuO and $CuAl_2O_4$ are also shown in Fig. 3(a). The edge energies (defined as the maximum in the first derivative of $\mu(E)$ with respect to energy) of CuO and $CuAl_2O_4$ were determined as 8983.3 eV and 8986.1 eV, respectively, in agreement with literature.[23,24] One of the features that clearly differentiates the XANES of CuO from that of $CuAl_2O_4$ is a shoulder in the edge step (absent for $CuAl_2O_4$). From the inset 3(a1) of Fig. 3(a) it can be seen that the shoulders in the edge step of CuAlNa0 and CuAlNa1 are less pronounced than for pure, *i.e.* unsupported CuO. This feature in the XANES of CuAlNa0 and CuAlNa1 can be attributed to the presence of a $CuAl_2O_4$ phase in these materials (as confirmed by XRD, Fig. 2). On the other hand, except for a minor reduction in the intensity of the white line (inset 3(a2)), the XANES spectra of CuAlNa3 and CuAlNa5 resemble very well the reference spectra of CuO. Linear combination fitting (LCF) of the XANES data (weight fractions of CuO and $CuAl_2O_4$ on an $Al_2O_3$ free basis, Table 1) shows that the quantity of $CuAl_2O_4$ in the materials decreased with increasing $Na^+$ content.

The experimentally determined $k^3$-weighted EXAFS functions of the synthesized oxygen carriers, CuO and $CuAl_2O_4$ are given in Fig. 3(b). The EXAFS functions of CuAlNa0, CuAlNa1 and CuAlNa3 show a reduction of the amplitude of the oscillations when compared to the CuO reference data (*e.g.* see inset 3(b1)). Moreover, the EXAFS spectra of CuAlNa0, CuAlNa1 and CuAlNa3 contain features that can be ascribed to $CuAl_2O_4$. These observations indicate that the (volume averaged) local environment of Cu in CuAlNa0, CuAlNa1 and CuAlNa3 is, due to the presence of $CuAl_2O_4$, somewhat different from pure CuO (in agreement with XRD and LCF analysis). On the other hand, the EXAFS data show that only CuAlNa5 has a similar signature as the CuO reference, indicating that 5 wt% $Na^+$ prevented the reaction between CuO and $Al_2O_3$.

Scanning electron micrographs of the synthesized oxygen carriers are given in Fig. S3 (ESI†). The oxygen carriers CuAlNa0 and CuAlNa1 reveal a porous surface morphology

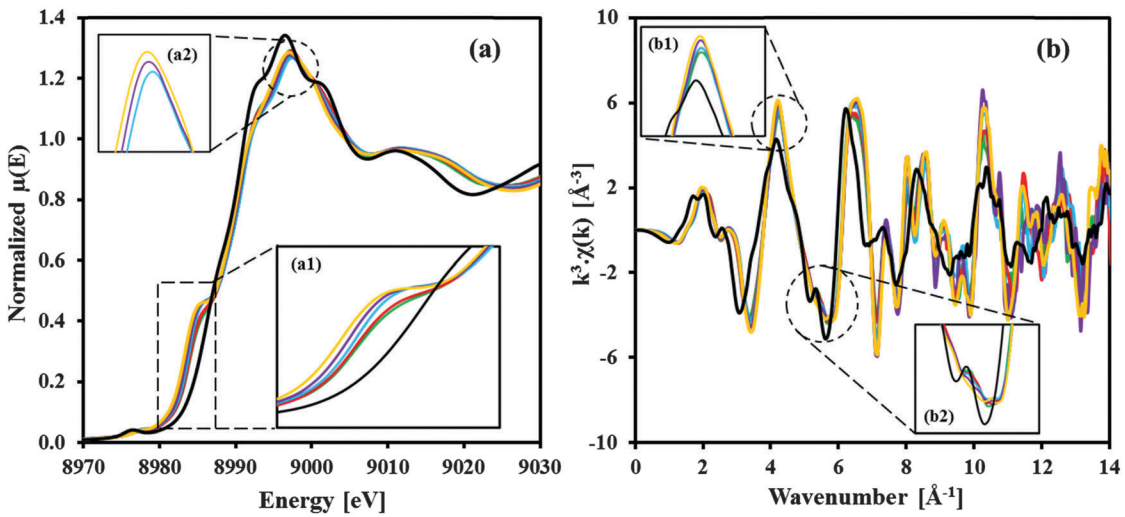


Fig. 3 Room temperature (a) XANES and (b) EXAFS spectra ($k^3$-weighted) of calcined (—) CuAlNa0, (—) CuAlNa1, (—) CuAlNa3, (—) CuAlNa5, (—) CuO and (—) $CuAl_2O_4$ measured at the Cu K-edge.

(in combination with a comparatively high surface area, Table S2, ESI†). Increasing the $Na^+$ content to 5 wt% led to a densification of the material's morphology. As expected, this change in morphology of CuAlNa3 and CuAlNa5 was accompanied by a decrease in surface area.

### Temperature programmed reduction

To determine the influence of $Na^+$ on the oxygen uncoupling characteristics of the synthesized oxygen carriers, $N_2$-TPR experiments were performed in a TGA. The normalized weight loss is plotted as a function of temperature for the different materials (Fig. 4). Fig. 4 confirms that the reduction of all oxygen carriers (defined as the temperature at which the oxygen carrier has lost 2% of the total weight loss) starts at ~770 °C, independent of the $Na^+$ loading. As expected, the reduction of CuAlNa0, CuAlNa1 and CuAlNa3 occurred in two steps. In the first step (temperature range 750–890 °C), CuO is reduced to $Cu_2O$ *via*:

$$4CuO(s) \rightarrow 2Cu_2O(s) + O_2(g) \quad (5)$$

The comparatively slow reduction of $CuAl_2O_4$ to $CuAlO_2$ occurs in the second step (temperature range 890–1050 °C), according to:

$$4CuAl_2O_4(s) \rightarrow 4CuAlO_2(s) + 2Al_2O_3(s) + O_2(g) \quad (6)$$

The (apparent) rate of $CuAl_2O_4$ reduction was slower in CuAlNa1 compared to CuAlNa0. Currently we cannot unequivocally explain the slower reduction of $CuAl_2O_4$ in CuAlNa1. XRD analysis of the reduced CuAlNa0, CuAlNa1 and CuAlNa3 confirmed the presence of $Cu_2O$, $CuAlO_2$ and $Al_2O_3$ (Fig. S4 of the ESI†). Due to the absence of $CuAl_2O_4$, the reduction of CuAlNa5 occurred in a single step. The X-ray diffractogram of reduced CuAlNa5 shows peaks due to $Cu_2O$ and $NaAlO_2$ only. The CuO content of the synthesized oxygen carriers, as determined from $N_2$-TPR experiments, was close to the theoretically expected value of 70 wt%, see Table 2.

$H_2$-TPR experiments, Fig. 5(a), were performed to study the effect of $Na^+$ on the reduction characteristics of the synthesized materials. The peak positions of the $H_2$-TPR profiles are summarized in the inset of Fig. 5(a). For CuAlNa0 and CuAlNa1, the reduction started at ~245 °C, with peaks located at ~310 °C and ~322 °C, respectively. A second peak was located at ~415 °C and ~385 °C for, respectively, CuAlNa0 and CuAlNa1. The first peak can be assigned to the reduction of CuO to Cu, whereas the second peak corresponds to the reduction of $CuAl_2O_4$ to Cu and $Al_2O_3$. For CuAlNa3 and CuAlNa5, reduction started at ~280 °C with peaks located at ~332 °C and ~335 °C, respectively. The presence of only a single peak in the $H_2$-TPR profiles of CuAlNa3 and CuAlNa5 is indicative of the absence of $CuAl_2O_4$ in these oxygen carriers. Overall, we observed that increasing $Na^+$ loadings led to increasing reduction temperatures. X-ray diffractograms of the reduced materials confirmed the presence of Cu in the reduced oxygen carriers (Fig. S5, ESI†). In the case of CuAlNa5, also $NaAlO_2$ was identified in the reduced materials (minor phase).

Table 2 CuO content of the oxygen carriers as determined from $N_2$-TPR

| Material | CuAlNa0 | CuAlNa1 | CuAlNa3 | CuAlNa5 |
|---|---|---|---|---|
| CuO content [wt%] | 70.4 | 69.9 | 71.1 | 70.9 |

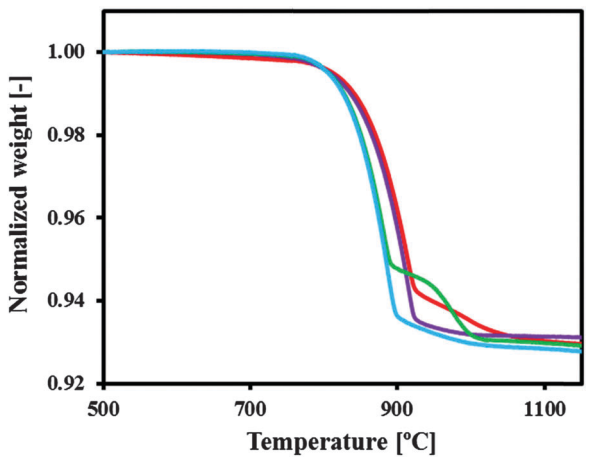


Fig. 4 $N_2$-TPR profiles of the synthesized oxygen carriers: (—) CuAlNa0, (—) CuAlNa1, (—) CuAlNa3 and (—) CuAlNa5.

The reduction and carbon deposition characteristics of the synthesized oxygen carriers were assessed further using $CH_4$-TPR. The $CH_4$-TPR profiles of the synthesized oxygen carriers are plotted in Fig. 5(b). The reduction of CuAlNa0 started at ~530 °C and was completed at ~710 °C. In contrast to the $N_2$-TPR and $H_2$-TPR measurements, we could not observe a separate reduction step for $CuAl_2O_4$ in the $CH_4$-TPR measurements. This indicates that using $CH_4$, CuO and $CuAl_2O_4$ are reduced simultaneously. The reduction of $Na^+$ doped oxygen carriers started at ~560 °C irrespective of the $Na^+$ content, *i.e.* at a higher temperature (+30 °C) compared to the undoped material. For CuAlNa0, a substantial increase in weight was observed for temperatures >750 °C. This is due to the deposition of coke *via* the $CH_4$ decomposition reaction, *viz.*:

$$CH_4(g) \rightarrow C(s) + H_2(g) \quad (7)$$

On the other hand, CuAlNa1 revealed a comparatively low propensity to coke formation and compared to CuAlNa0, the onset of carbon deposition was shifted to higher temperatures. Transmission electron microscopy (Fig. S6, ESI†) revealed that the carbon deposited on CuAlNa0 and CuAlNa1 was in the form of filaments and whiskers. Importantly, no carbon deposition was observed in the transmission electron micrographs of CuAlNa3 and CuAlNa5; a very favourable characteristic for CLC. The increased resistance of $Na^+$-doped oxygen carriers to carbon formation is attributed to the ability of alkali metals to stabilize preferably $CH_x$–* species instead of C–* surface intermediates.[25,26] The X-ray diffractograms of the $CH_4$-reduced oxygen carriers showed peaks due to Cu (Fig. S7, ESI†). For CuAlNa5, Bragg reflections due to $NaAlO_2$ were also identified.

### CLC and CLOU performance

The cyclic CLOU and CLC performance of the synthesized oxygen carriers was evaluated in a TGA at 900 °C. The normalized oxygen

 

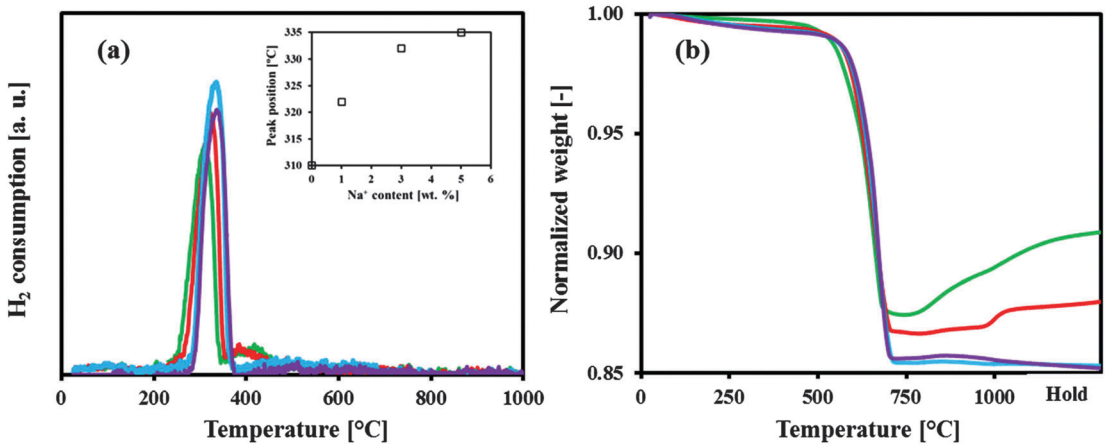


Fig. 5 (a) $H_2$- and (b) $CH_4$-TPR profiles of the synthesized oxygen carriers: (—) CuAlNa0, (—) CuAlNa1, (—) CuAlNa3 and (—) CuAlNa5.

carrying capacity defined as

$$\text{Normalized oxygen carrying capacity} = \frac{\text{measured weight loss}}{\text{theoretical weight loss}} \quad (8)$$

is plotted in Fig. 6(a) (CLOU) and (b) (CLC) as a function of cycle number. Under CLOU conditions the normalized oxygen carrying capacity of CuAlNa0 and CuAlNa1 decreased with cycle number. This behaviour is due to the slow oxidation kinetics of $CuAlO_2$ back to $CuAl_2O_4$.[4] Over the 20 cycles tested a ~16% decrease in the oxygen carrying capacity was observed for CuAlNa0 and CuAlNa1. Doping the oxygen carrier with 1 wt% $Na^+$ did not prevent the formation of a solid solution between CuO and $Al_2O_3$ (as confirmed by XRD and XAS). Thus, the CLOU performances of CuAlNa0 and CuAlNa1 are very similar. In the X-ray diffractogram of cycled (oxidized state) CuAlNa0 and CuAlNa1, CuO, $CuAlO_2$ and $Al_2O_3$ were identified (Fig. S8, ESI†). On the other hand, for CuAlNa3 and CuAlNa5 the oxygen carrying capacity is only reduced by ~3% over the first four cycles. From the fifth cycle onwards, the oxygen carrying capacity of CuAlNa3 remained stable, reaching 97% of the theoretically predicted oxygen carrying capacity of the material. The X-ray diffractogram of cycled CuAlNa3 (Fig. S8, ESI†) showed weak peaks due to $CuAl_2O_4$ along with CuO and $NaAlO_2$. This confirms (in line with XAS data) that doping CuO–$Al_2O_3$ with 3 wt% $Na^+$ is not sufficient to completely avoid the formation of a solid solution between CuO and $Al_2O_3$. In the case of CuAlNa5, the normalized oxygen carrying capacity reached 100% of the theoretically predicted oxygen carrying capacity in the ninth cycle and remained stable for the subsequent cycles. This implies a fully reversible reduction–oxidation of the CuO–$Cu_2O$ couple. The X-ray diffractogram of cycled (oxidized state) CuAlNa5 showed peaks due to CuO and $NaAlO_2$ only, *i.e.* the spinel $CuAl_2O_4$ is not present in CuAlNa5. The slight drop in the oxygen carrying capacity during the first five cycles is probably due to some small changes in the kinetics of the oxidation reaction over the initial CLOU cycles, as shown in Fig. S9 (ESI†).

Turning to the CLC performance of the synthesized oxygen carriers, a gradual decrease in the normalized oxygen carrying capacity was observed for CuAlNa0 (Fig. 6(b)). On the other hand, all $Na^+$ doped oxygen carriers showed stable oxygen carrying capacities close to 1 over the 20 redox cycles tested. The X-ray diffractograms of cycled (oxidized state) CuAlNa0 and

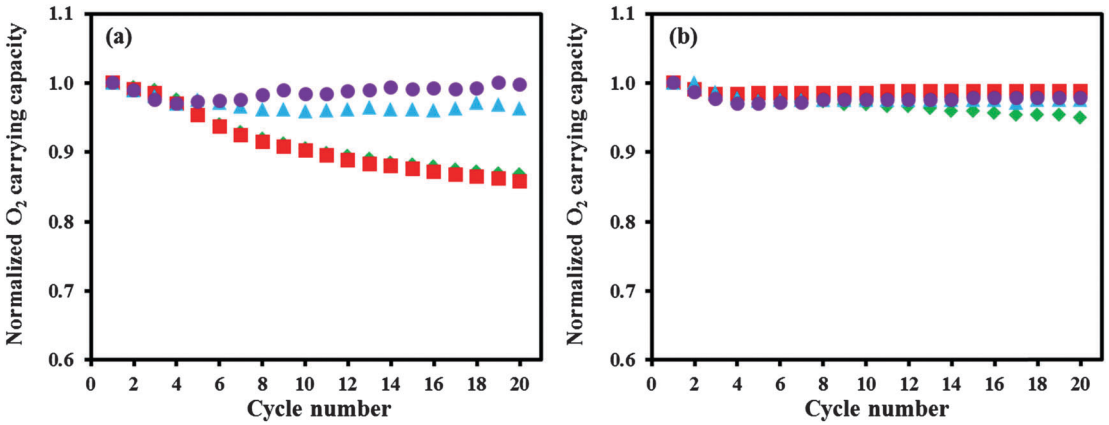


Fig. 6 Normalized oxygen carrying capacity of the oxygen carriers synthesized, as determined in a TGA at 900 °C under (a) CLOU and (b) CLC conditions: (◆) CuAlNa0, (■) CuAlNa1, (▲) CuAlNa3 and (●) CuAlNa5.

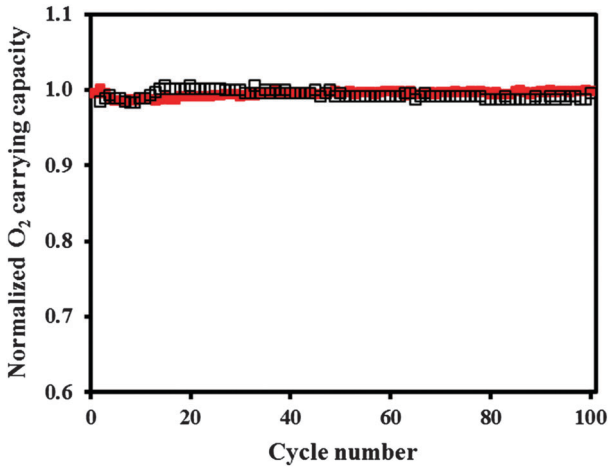


Fig. 7 Normalized oxygen carrying capacity of CuAlNa5, as determined in a TGA at 900 °C under (■) CLC and (□) CLOU conditions.

CuAlNa1, see Fig. S10 (ESI†), showed reflections due to CuO and $CuAl_2O_4$. On the other hand, the XRD data of CuAlNa3 and CuAlNa5 XRD showed only peaks due to CuO and $NaAlO_2$. It should be noted that $CuAl_2O_4$ is fully reducible under CLC conditions and does not reduce the oxygen carrying capacity of CuAlNa0.[10,14] On the other hand, the temporally resolved mass loss profiles of CuAlNa0 (Fig. S11, ESI†) reveal that the rate of oxidation of CuAlNa0 decreased with cycle number, leading in turn to a decreasing oxygen carrying capacity with cycle number (the oxidation time was fixed to 390 s). In contrast, all $Na^+$ doped oxygen carriers not only possessed higher oxidation rates (compared to undoped material) but also maintained their high oxidation rates over the 20 cycles tested. Therefore, CuAlNa1, despite containing $CuAl_2O_4$, showed a stable cyclic oxygen carrying capacity under CLC conditions.

The long term redox stability of CuAlNa5 was evaluated further in a TGA at 900 °C for 100 CLC and CLOU cycles. Fig. 7 plots the normalized oxygen carrying capacity of CuAlNa5 under both CLC and CLOU conditions as a function of cycle number. Under both CLC and CLOU conditions CuAlNa5 showed stable oxygen carrying capacities close to 1 over the 100 redox cycles tested, indicating that there was no sodium leaching at the high operating temperatures. Even after 100 cycle, we could not observe $CuAl_2O_4$ or $CuAlO_2$ in the X-ray diffractograms (Fig. S12, ESI†) of cycled (oxidized state) CuAlNa5, confirming further the long term stability of $Na^+$-doped and $Al_2O_3$-stabilized CuO.

### *In situ* XANES spectroscopy

*In situ* XANES spectroscopy was performed to investigate the reduction pathways of undoped and $Na^+$-doped (5 wt%), $Al_2O_3$-stabilized CuO at 750 °C. In total three redox cycles were performed for each material. Fig. 8(a) and (b) show the temporal changes of the Cu K-edge XANES spectra of, respectively, CuAlNa0 and CuAlNa5 (first reduction step using 5 vol% $H_2$ in He). Each spectrum plotted was acquired in He after a 5 s pulse of the reducing gas was released into the bed. Fig. 8 reveals that at 750 °C the reduction of the oxygen carriers commenced with the first $H_2$ pulse, *i.e.* an induction period was not observed. The absence of an induction period at 750 °C is most likely due to the high thermal disorder in the materials as confirmed by the EXAFS spectra of CuAlNa0 and CuAlNa5 (Fig. S13 of the ESI†). Rodriguez *et al.*[27] argued that the occurrence of an induction period is related to the formation of defect sites on the metal oxide surface. These active sites have a high activity for the dissociation of $H_2$, but have, however, only been observed at low temperatures, *i.e.* $T < 310$ °C.[27] For example, the *in situ* XAS measurements of Kim *et al.*[15] showed an induction period in the temperature range 250–300 °C (commercial, pure CuO powder; 5 vol% $H_2$ in He with a flow rate $>15$ mL $min^{-1}$). Kim *et al.*[15] also reported that the duration of the induction period decreased with increasing temperature.

The reduction pathways of CuAlNa0 and CuAlNa5 (Fig. 9(a) and (b), respectively) were determined using LCF of the acquired XANES data. Fig. 9 confirms that the reduction of both oxygen

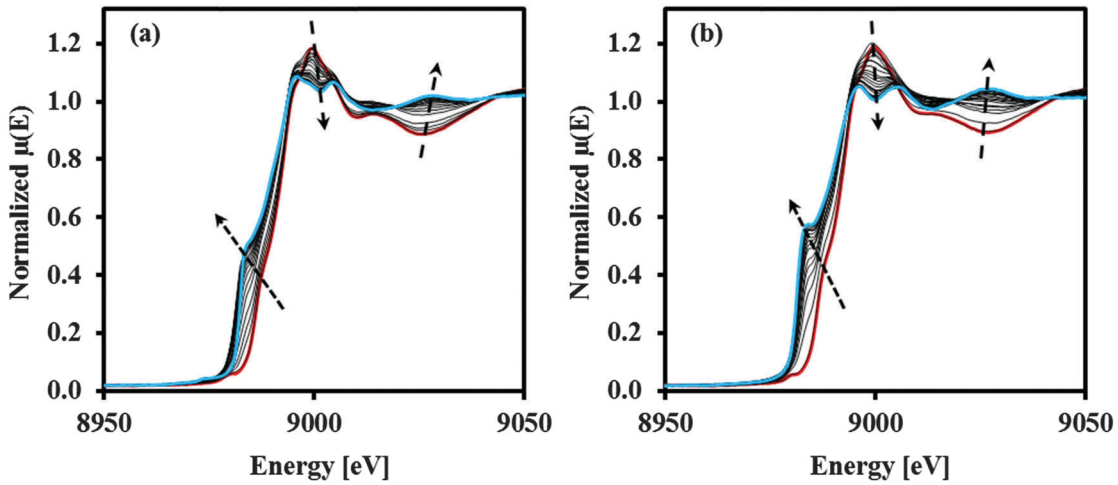


Fig. 8 Time-resolved (150 s) Cu K-edge XANES spectra during reduction (5 vol% $H_2$ in He) of (a) CuAlNa0 and (b) CuAlNa5 at 750 °C. The red (—) and blue (—) lines correspond to the initial and final states, respectively.

 

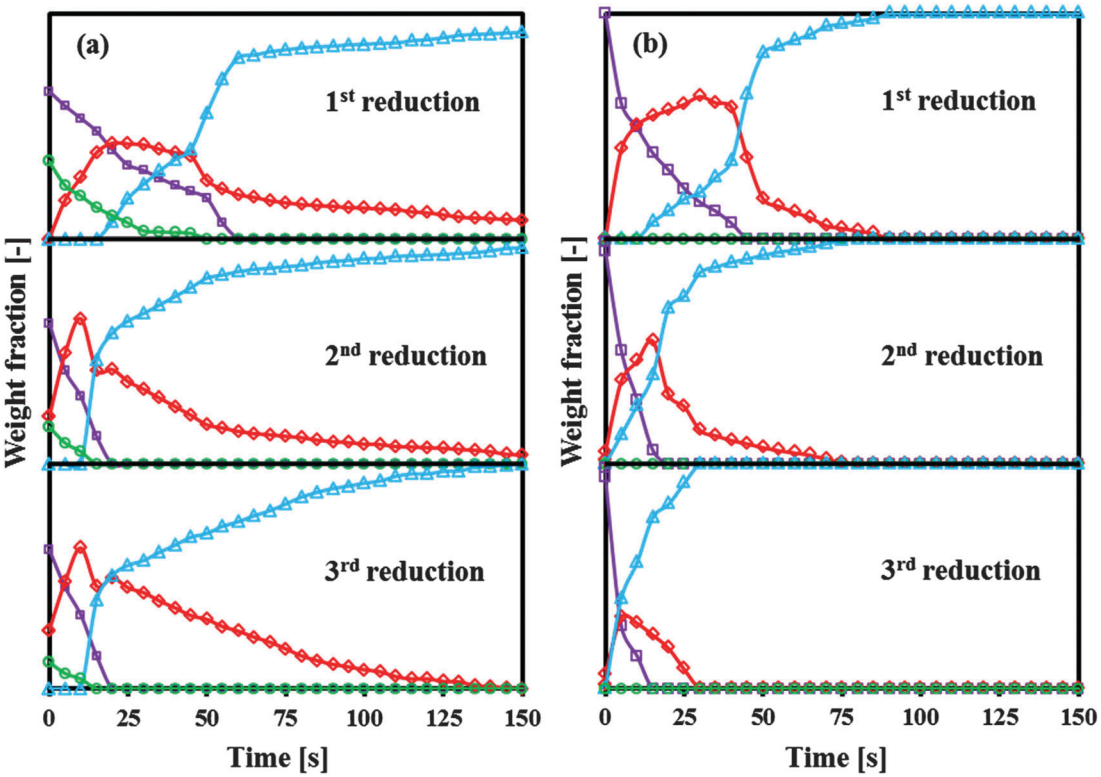


Fig. 9 Weight fractions of CuO (–□–), $CuAl_2O_4$ (–○–), $Cu_2O$ (–◊–) and Cu (–△–) during the reduction of (a) CuAlNa0 and (b) CuAlNa5 using linear combination fitting of the acquired Cu K-edge XANES data. The reduction was performed at 750 °C using 5 s pulses of 5 vol% $H_2$ and 95 vol% He. 30 $H_2$ pulses were used in total.

carriers proceeds *via* the $Cu_2O$ intermediate. The transition though the $Cu_2O$ intermediate phase during reduction was supported further by principal component analysis (PCA). PCA of the recorded XANES data of CuAlNa0 and CuAlNa5 confirmed that all spectra could be reconstructed when using the four reference compounds CuO, $CuAl_2O_4$, $Cu_2O$ and Cu. Using DFT, Kim *et al.*[15] showed that under reducing conditions CuO can reach metastable states that possess a large number of oxygen vacancies. A transition from these metastable states to $Cu_2O$ is associated with large variations in the cell parameters of CuO, whereas a very small amount of energy (total energy of unit cell calculated using DFT) is released during the transition from metastable CuO (CuO with large number of oxygen vacancies) to $Cu_2O$. Consequently, Kim *et al.*[15] proposed that $Cu_2O$ intermediates are only formed for slow reduction rates. On the other hand, under fast oxygen removal conditions the following transitions CuO → metastable CuO → Cu are favored energetically. We speculate that in the present work, the use of $H_2$ pulses (simulating a slow reduction) has allowed the formation of the $Cu_2O$ intermediate during reduction. We did not observe, within the temporal resolution of the XAS spectrometer, the formation of the $Cu_2O$ intermediate when a continuous flow of 25 mL $min^{-1}$ of 5 vol% $H_2$ in He was used for reduction (simulating a fast reduction).

The *in situ* XAS results plotted in Fig. 9(a) also show that in the first reduction segment of CuAlNa0, CuO and $CuAl_2O_4$ were reduced simultaneously to $Cu_2O$. The reduction of CuO and $CuAl_2O_4$ to $Cu_2O$ was completed within the first 60 s. The further reduction of $Cu_2O$ to Cu started after 20 s. At the end of the reduction step (150 s), the material still contained ~15 wt% $Cu_2O$, indicative of comparatively slow reduction rate for $Cu_2O$.

Nonetheless, XANES confirmed that CuO that is in a solid solution with $Al_2O_3$ is fully reducible to Cu *via* the $Cu_2O$ intermediate. Thus, the formation of $CuAl_2O_4$ does not reduce the oxygen carrying capacity of the synthesized oxygen carriers. The composition of CuAlNa0 at the end of the first redox cycle (*i.e.* after re-oxidation with 5 vol% $O_2$ in He) was 62.5 wt% CuO, 21.0 wt% $Cu_2O$ and 16.5 wt% $CuAl_2O_4$. The incomplete oxidation of $Cu_2O$ to CuO within the fixed oxidation time is due to the sluggish oxidation kinetics of the Cu(I)–Cu(II) transition.[28] In the reduction step of the second and third redox cycle, the reduction of CuO and $CuAl_2O_4$ was completed within 20 seconds, *i.e.* three times faster when compared to the first cycle. Similarly, the (apparent) rate of reduction of $Cu_2O$ also increased slightly with cycle number. As a consequence, $Cu_2O$ was fully reduced to Cu in the third cycle.

For CuAlNa5, only CuO was identified in the fresh and re-oxidized materials. In the first 15 s of the reduction segment of the first cycle, CuO was reduced primarily to $Cu_2O$; only a minor quantity of Cu was detected. After 15 s, the fraction of Cu started to increase gradually. The reduction of CuO and $Cu_2O$ was completed within 45 s and 90 s, respectively. Here, the apparent rate of reduction of CuO and $Cu_2O$ was again found to increase with cycle number. For example, in the

second and third cycle, Cu occurred already after the first $H_2$ pulse (5 s). Furthermore, we observed that for CuAlNa5 the quantity of $Cu_2O$ formed during reduction decreases with increasing cycle number. From Fig. 9(a) and (b) it is evident that the reduction kinetics of CuAlNa5 are faster compared to CuAlNa0. The influence of $Na^+$ on the reduction pathways and kinetics will be discussed in detail further below.

To explain the increase in the reduction kinetics with cycle number, room temperature EXAFS data of fresh and cycled CuAlNa5 were recorded. Compared to fresh CuAlNa5, the Fourier transformed EXAFS function of cycled CuAlNa5 shows an appreciably reduced height of the peaks due to the first and second coordination spheres (Fig. S14, ESI†), indicative of an increasing defect structure in CuO with cycle number. Fitting of the first shell of cycled CuAlNa5 shows an increase in the Debye–Waller factor and a decrease in the Cu–O coordination number compared to fresh CuAlNa5 (Table S4, ESI†).

### Conductivity measurements

Using DFT calculations, Li *et al.*[29,30] argued that the redox performance of transition metal oxides depends critically on the activation energy for the counter-current conduction of ions and electrons through the oxygen carrier. However, there is currently very little experimental evidence available to support this modelling result. In order to investigate the influence of $Na^+$ doping on the activation energy for charge transport 4-point electrical conductivity measurements were performed. In Fig. 10(a) the measured resistivity of CuAlNa0 and CuAlNa5 is plotted as a function of temperature. CuAlNa5 has a lower resistivity than CuAlNa0 and the resistivity decreases with increasing temperature. The resistivity data was further analysed by fitting the following Arrhenius relationship

$$\sigma = \frac{\sigma_0}{T}\exp\left(-\frac{E_a}{kT}\right) \quad (9)$$

where, $\sigma_0$, $E_a$ and $k$ are, respectively, a proportionality constant, the activation energy for charge conduction and the Boltzmann constant. Plotting $\ln(\sigma T)$ as a function of $1/T$ yielded two distinct regions (Fig. S15, ESI†). Thus, the low and high temperature regimes were fitted by separate activation energies. For temperatures $<600$ °C, the activation energy for charge transport in CuAlNa0 and CuAlNa5 was determined as 0.152 eV and 0.098 eV, respectively (see Fig. 10(b)). At $\sim$600 °C, an increase in activation energy is observed, indicative of a change in the charge transport mechanism. For temperatures exceeding 600 °C, an activation energy of 0.448 and 0.405 eV was determined for CuAlNa0 and CuAlNa5, respectively. It is worth noting here that CuO is a p-type semiconductor.[31] Jeong and Choi[32] showed that conduction at low temperature is due to the hopping of charge carriers in metal deficient CuO, *i.e.* $Cu_{1-y}O$. Using 4-point conductivity measurements, Jeong and Choi[32] determined the activation energy for charge carrier hopping as $0.1 \pm 0.01$ eV which is in good agreement with the values obtained here (for $T < 600$ °C). The high temperature region gives the intrinsic conductivity of the material. In the literature the activation energy for charge transport through unsupported CuO at high temperatures (for $T > 600$ °C) was determined as $0.7 \pm 0.04$ eV. This value is slightly higher than the one obtained from our measurements. The difference can most likely be attributed to morphological difference between commercial CuO and the material synthesized by us.[32]

## Discussion

### Effect of $Na^+$ on the morphological properties of $Al_2O_3$-stabilized CuO

We observe that the average crystallite size of CuO in the synthesized oxygen carriers is not affected by $Na^+$ doping (Table 1). This implies that $Na^+$ doping has no pronounced solute drag or strain effect on the crystallite size development of CuO.[33] On the other hand, $Na^+$ doping significantly modifies the surface morphology of the oxygen carriers synthesized (Fig. S3, ESI†). Based on visual inspection of the electron micrographs, the sintering tendency of the grains was found to increase with increasing $Na^+$ content. It has been reported

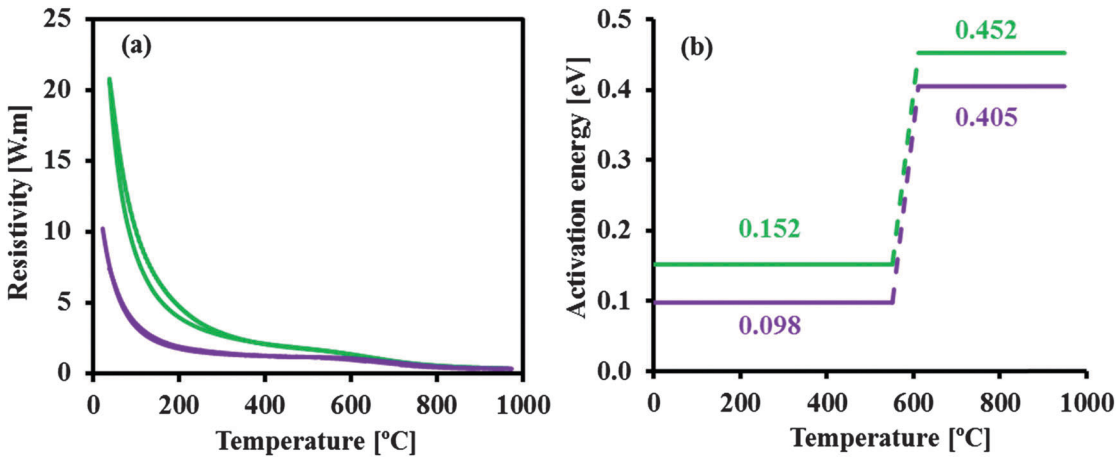


Fig. 10 (a) Resistivity as a function of temperature for CuAlNa0 (—) and CuAlNa5 (—); (b) activation energy for charge transport for CuAlNa0 (—) and CuAlNa5 (—).

 

that the addition of alkali metals, *e.g.* Li, to metal oxides, *e.g.* ceria, can increase sintering through an increased atomic mobility at the grain boundaries.[34]

### Influence of $Na^+$ on reduction kinetics and charge transport characteristics

From *in situ* XANES spectroscopy results (Fig. 9) it is evident that the (apparent) rate of reduction of CuAlNa5 is appreciably faster when compared to CuAlNa0, albeit the same reduction pathway was followed, *viz.* CuO → $Cu_2O$ → Cu. As the oxygen carrier CuAlNa5 has a smaller surface area than CuAlNa0 (Table S2, ESI†) the faster reduction kinetics of CuAlNa5 cannot be explained by surface area effects. Thus, we attribute the fast reduction kinetics of CuAlNa5 to $Na^+$ induced defect structures. Owing to differences in the oxidation states and ionic radii of Cu ions (0.73 Å) and Na ions (1.02 Å), doping $Al_2O_3$-stabilized CuO with $Na^+$ creates aliovalent substitution defects in the oxygen carrier.[35] Aliovalent substitution defects lower the positive charge within the oxygen carrier, therefore, oxygen vacancies or holes are generated as a charge compensation mechanism to maintain the overall charge neutrality. These oxygen vacancies or holes facilitate the transport of oxygen ($O^{2-}$) and electronic carriers during redox reactions. Comparing the electrical transport characteristics of $Na^+$ doped CuO (CuAlNa5) and undoped CuO (CuAlNa0), it is clear that $Na^+$ doping increases the reduction kinetics of CuO by (i) lowering the activation energy for charge transport by ~0.05 eV and (ii) increasing the overall conductivity by a factor of 2. We ascribe the lowering of the activation energy for charge transport to $Na^+$ induced modifications in the electronic structure of CuO in line with XANES data and the absence of a spinel phase in CuAlNa5.

### Influence of cycle number on the reduction kinetics

Fig. 9 shows that the reduction kinetics of both CuAlNa0 and CuAlNa5 increase with cycle number. This observation is consistent with the TGA and fluidized bed measurements of Imtiaz *et al.*[10,11] that also showed an increasing reduction rate of $Al_2O_3$-stabilized CuO with cycle number. The Fourier transformed EXAFS functions of fresh and cycled CuAlNa5 (Fig. S14 and Table S4, ESI†) revealed that the number of defects (*e.g.* oxygen vacancies) in the CuO structure increase with number of repeated redox cycles resulting in an increasing distortion of the local atomic order. We believe that the increasing structural disorder of CuO with cycle number facilitates the transport of oxygen ions during reduction, which in turn leads to faster reduction kinetics.

### Relation between reduction kinetics and pathways

The quantity of $Cu_2O$ formed during the reduction of CuAlNa5 was found to decrease with increasing cycle number (*in situ* XAS measurements, Fig. 9(b)). The decreasing quantity of $Cu_2O$ with cycle number suggests a change in the reduction pathway from a sequential (CuO → $Cu_2O$ → Cu) to a direct transition (CuO → Cu). Indeed, it is conceivable that the increasing (apparent) reduction kinetics with cycle number as discussed above, are a direct consequence of this change in reduction pathway with cycle number. This observation is an agreement with the report of Kim *et al.*[15] that showed that the reduction kinetics of pure CuO plays an important role for the reduction pathway. The sequential reduction of CuO occurs only under slow oxygen removal conditions. Therefore, an increasing rate of reduction with cycle number (as observed here) would favour the CuO → Cu transition and change the reduction pathway from sequential to direct. The change of the reduction pathway of CuO would have important consequences for the oxidation mechanism of gaseous hydrocarbons. In the case of a sequential reduction pathway the reaction between $CH_4$ and CuO proceeds with both the lattice oxygen of CuO and molecular oxygen released *via* the CuO → $Cu_2O$ transition. For the direct reduction of CuO, only lattice oxygen will be available for the oxidation of $CH_4$.

## Conclusions

In this work, we probe and characterize in detail the effect of $Na^+$ doping on the local structure, electronic properties and cyclic redox characteristics of $Al_2O_3$-stabilized CuO. Using a combination of XAS, XRD and conductivity measurements we could demonstrate that the improved redox performance of $Na^+$ doped oxygen carriers under CLC conditions is due to $Na^+$ induced changes in the electronic structure of CuO and the suppression of the formation of a spinel phase. These structural changes lead to enhanced electronic transport kinetics possibly due to the generation of oxygen vacancies compensating the lower charge of $Na^+$ when compared to $Cu^{2+}$. The absence of the $CuAl_2O_4$ phase leads to a high redox stability under CLOU conditions. Utilizing *in situ* XANES spectroscopy, we were able to show that the reduction of both undoped and doped CuO proceeds *via* the $Cu_2O$ intermediate. The (apparent) rate of reduction increases with cycle number owing to an increasing structural disorder. As a consequence, with cycle number the reduction pathway changes from sequential (CuO → $Cu_2O$ → Cu) to a direct CuO → Cu transition.

## Acknowledgements

We are grateful to the Swiss National Science Foundation (SNF) (Project 406640_13670011) for financial support. We also thank Mrs Lydia Zehnder for her help with the XRD analysis and the Scientific Centre for Optical and Electron Microscopy (ScopeM) for providing access to and training on scanning and transmission electron microscopes. We acknowledge SNBL and ESRF for the provision of beamtimes.

## Notes and references

1 Q. Imtiaz, D. Hosseini and C. R. Muller, *Energy Technol.*, 2013, **1**, 633–647.
2 R. K. Lyon and J. A. Cole, *Combust. Flame*, 2000, **121**, 249–261.

3 P. Gayan, I. Adanez-Rubio, A. Abad, L. F. de Diego, F. Garcia-Labiano and J. Adanez, *Fuel*, 2012, **96**, 226–238.
4 M. Arjmand, A. M. Azad, H. Leion, T. Mattisson and A. Lyngfelt, *Ind. Eng. Chem. Res.*, 2012, **51**, 13924–13934.
5 M. M. Hossain and H. I. de Lasa, *Chem. Eng. Sci.*, 2008, **63**, 4433–4451.
6 J. Adanez, A. Abad, F. Garcia-Labiano, P. Gayan and L. F. de Diego, *Prog. Energy Combust. Sci.*, 2012, **38**, 215–282.
7 I. Barin and O. Knacke, *Thermochemical properties of inorganic substances*, Springer-Verlag, Berlin, New York, 1973.
8 K. T. Jacob and C. B. Alcock, *J. Am. Ceram. Soc.*, 1975, **58**, 192–195.
9 S. Y. Chuang, J. S. Dennis, A. N. Hayhurst and S. A. Scott, *Combust. Flame*, 2008, **154**, 109–121.
10 Q. Imtiaz, A. M. Kierzkowska and C. R. Muller, *ChemSusChem*, 2012, **5**, 1610–1618.
11 Q. Imtiaz, M. Broda and C. R. Muller, *Appl. Energy*, 2014, **119**, 557–565.
12 M. Houalla, J. Lemaitre and B. Delmon, *J. Chem. Soc., Faraday Trans. 1*, 1982, **78**, 1389–1400.
13 G. A. Elshobaky, T. Elnabarawy, G. A. Fagal and N. H. Amin, *Thermochim. Acta*, 1989, **141**, 195–203.
14 Q. Imtiaz, A. M. Kierzkowska, M. Broda and C. R. Muller, *Environ. Sci. Technol.*, 2012, **46**, 3561–3566.
15 J. Y. Kim, J. A. Rodriguez, J. C. Hanson, A. I. Frenkel and P. L. Lee, *J. Am. Chem. Soc.*, 2003, **125**, 10684–10692.
16 A. M. Kierzkowska, C. D. Bohn, S. A. Scott, J. P. Cleeton, J. S. Dennis and C. R. Muller, *Ind. Eng. Chem. Res.*, 2010, **49**, 5383–5391.
17 S. Brunauer, P. H. Emmett and E. Teller, *J. Am. Chem. Soc.*, 1938, **60**, 309–319.
18 E. P. Barrett, L. G. Joyner and P. P. Halenda, *J. Am. Chem. Soc.*, 1951, **73**, 373–380.
19 J. L. M. Rupp, E. Fabbri, D. Marrocchelli, J. W. Han, D. Chen, E. Traversa, H. L. Tuller and B. Yildiz, *Adv. Funct. Mater.*, 2014, **24**, 1562–1574.
20 A. A. Felix, J. L. M. Rupp, J. A. Varela and M. O. Orlandi, *J. Appl. Phys.*, 2012, **112**, 054512.
21 B. Ravel and M. Newville, *J. Synchrotron Radiat.*, 2005, **12**, 537–541.
22 A. L. Patterson, *Phys. Rev.*, 1939, **56**, 978–982.
23 E. Kleymenov, J. Sa, J. Abu-Dahrieh, D. Rooney, J. A. Van Bokhoven, E. Troussard, J. Szlachetko, O. V. Safonova and M. Nachtegaal, *Catal.: Sci. Technol.*, 2012, **2**, 373–378.
24 V. V. Galvita, M. Filez, H. Poelman, V. Bliznuk and G. B. Marin, *Catal. Lett.*, 2014, **144**, 32–43.
25 A. P. E. York, T. C. Xiao, M. L. H. Green and J. B. Claridge, *Catal. Rev.*, 2007, **49**, 511–560.
26 J. R. Rostrup-Nielsen, in *Catalysis: Science and Technology*, ed. J. R. Anderson and M. Boudart, Springer-Verlag, Berlin Heidelberg, vol. 5, ch. 1, 1984.
27 J. A. Rodriguez, J. C. Hanson, A. I. Frenkel, J. Y. Kim and M. Perez, *J. Am. Chem. Soc.*, 2002, **124**, 346–354.
28 S. Y. Chuang, J. S. Dennis, A. N. Hayhurst and S. A. Scott, *Energy Fuels*, 2010, **24**, 3917–3927.
29 F. X. Li, Z. C. Sun, S. W. Luo and L. S. Fan, *Energy Environ. Sci.*, 2011, **4**, 876–880.
30 F. X. Li, S. W. Luo, Z. C. Sun, X. G. Bao and L. S. Fan, *Energy Environ. Sci.*, 2011, **4**, 3661–3667.
31 X. Y. Song, S. X. Sun, W. M. Zhang, H. Y. Yu and W. L. Fan, *J. Phys. Chem. B*, 2004, **108**, 5200–5205.
32 Y. K. Jeong and G. M. Choi, *J. Phys. Chem. Solids*, 1996, **57**, 81–84.
33 E. Zolotoyabko, J. L. M. Rupp and L. J. Gauckler, *Scr. Mater.*, 2012, **66**, 190–193.
34 J. D. Nicholas and L. C. De Jonghe, *Solid State Ionics*, 2007, **178**, 1187–1194.
35 R. D. Shannon, *Acta Crystallogr.*, 1976, **32**, 751–767.

 